


 Cite this: *RSC Adv.*, 2021, 11, 23975

Highly sensitive detection of nitrobenzene by a series of fluorescent 2D zinc(II) metal–organic frameworks with a flexible triangular ligand†

 Xue Yang, Yixia Ren,[✉] Hongmei Chai, Xiufang Hou,^{*} Zhixiang Wang and Jijiang Wang^{ID}

Four fluorescent zinc(II) metal–organic frameworks, namely [Zn(HCIA)(4,4'-bipy)] (1), [Zn₂(CIA)(OH)(1,4-bibz)_{1.5}·H₂O] (2), [Zn(CIA)(OH)(4,4'-bbpy)] (3), and [Zn₂(HCIA)(4,4'-bimp)·H₂O] (4), were prepared hydrothermally with a flexible triangular ligand (H₃CIA) and a series of linear N-donor ligands (H₃CIA = 5-(2-carboxybenzyloxy) isophthalic acid, 4,4'-bipy = 4,4'-bipyridine, 1,4-bibz = 1,4-bis(1-imidazolyl)benzene; 4,4'-bbpy = 4,4'-bis(imidazolyl)biphenyl; 4,4'-bimp = 4,4'-bis(imidazole-1-ylethyl)biphenyl). Structural analyses revealed that complex 1 exhibited a 2D brick-like network structure based on the basic bimetallic ring, 2 was also a 2D interspersed structure from the 1D tubular structure, compound 3 possessed a 2D (4,4) network with 4,4'-bbpy occupying the holes, and complex 4 displayed a 2D network from the 1D ladder-like chain. The thermal stabilities and fluorescent properties of these complexes were investigated in the solid state. The fluorescent sensing experiments revealed that all Zn-MOFs could highly sensitively detect nitrobenzene in aqueous solution, which indicated that these materials can be used as fluorescent probes for the detection of nitrobenzene.

 Received 13th May 2021
 Accepted 15th June 2021

DOI: 10.1039/d1ra03737d

rsc.li/rsc-advances

Introduction

Metal–organic frameworks (MOFs) have seen much rapid development in recent years, with interest derived from their structural variability and many functional applications including fluorescence sensors,¹ magnetism,² gas adsorption and exchange,³ and heterogeneous catalysis.⁴ As fluorescence materials, luminescence MOFs have been employed to detect metal ions,⁵ anions,⁶ organic solvents,⁷ antibiotics,⁸ pollutants,⁹ pesticides,¹⁰ and some small molecules¹¹ with a high selectivity and sensitivity because of their advantages of adjustable pore sizes and variable functional groups. Fluorescence sensor investigations based on MOFs have mainly centered on lanthanide-MOFs (Ln = Eu³⁺ and Tb³⁺) and transition metal MOFs (Zn²⁺ and Cd²⁺) in recent years.¹² Nitrobenzene (NB) is a widely used organic synthesis intermediate in the organic synthesis industry, but its high toxicity to humans has inspired the development of rapid detection methods and experiments for it. Various detection methods for NB have been developed,

such as gas chromatography, high-performance liquid chromatography (HPLC), and electrochemical analysis.¹³ However compared with these analysis methods, fluorescent probes based on MOFs being developed to detect NB are showing increasing advantages including structural design ability, pore size tenability, host–guest interaction, and stable luminescence. A large number of fluorescent Ln-MOF probes for the detection of nitrobenzene have been discovered, and several Zn/Cd-MOF probes have been used to detect nitrobenzene.¹⁴

Zn-MOFs are a class of rapidly developing MOF materials thanks to the simple and controllable coordination conditions of the zinc(II) ion, stable and microporous frameworks, and excellent fluorescence properties.¹⁵ Rigid or flexible organic ligands containing carboxyl groups are frequently used in the formation of Zn-MOFs, especially multi-carboxylate ligands such as 5-(2-carboxybenzyloxy) isophthalic acid (H₃CIA), a flexible tri-carboxylate ligand with three carboxyl groups, which are more favorable for the coordination behavior with metal ions. Only a dozen MOFs based on the H₃CIA ligand with Ni²⁺, Cd²⁺, Ln³⁺, and Zn²⁺ ions have been reported and these have exhibited diverse forms, structures, and properties.¹⁶ Based on the above research background, we tried to design a series of zinc-MOFs with the H₃CIA ligand and four long-chain N-donor ligands (Chart 1), which we obtained as single crystals, and then used these to investigate their structural features and sensing properties toward nitrobenzene in aqueous solution.

College of Chemistry and Chemical Engineering, Laboratory of New Energy and New Function Materials, Shaanxi Key Laboratory of Chemical Reaction Engineering, Yan'an University, Yan'an, 716000, P. R. China. E-mail: renyixia1@163.com; houxf1977@126.com

† Electronic supplementary information (ESI) available: Bond lengths and bond angles data table, TG curves, PXRD patterns, the emission of the free ligands, Fluorescence time diagrams. CCDC numbers of complexes 1–4 are 2046401–2046404. For ESI and crystallographic data in CIF or other electronic format see DOI: 10.1039/d1ra03737d



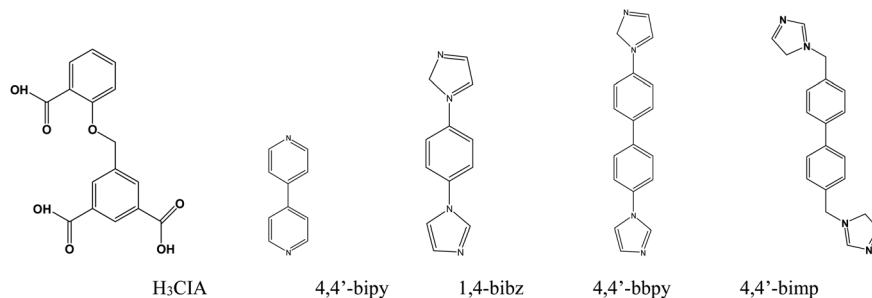


Chart 1 Structural representation of the ligands used in complexes 1–4.

Experimental

Materials and measurements

All the solvents and reagents were commercially available. Thermogravimetric analysis was performed using a NETZSCH STA 449C microanalyzer heated from 30 °C to 900 °C in an air atmosphere. The fluorescence spectra were determined by F-7100 fluorescence spectrophotometer at room temperature. Element analysis of the C, N, H, and O elements was performed using a Flash 2000 organic element analyzer. Powder X-ray diffraction (PXRD) patterns were obtained using a Rigaku Ultima IV diffractometer. The characteristic absorption peak of the MOFs was obtained by comparing the infrared spectrum with the standard infrared spectrum. The theoretical calculation was performed by Density Functional Theory (DFT).

Synthesis

[Zn(HCIA)(4,4'-bipy)] (1). ZnSO₄·7H₂O (0.029 g), H₃CIA (0.016 g), and 4,4'-bipy (0.015 g) were mixed with 3 mL water and 0.3 mL NaOH (0.065 mol L⁻¹) in a 25 mL Teflon-lined stainless steel container and heated at 160 °C for 72 h. The final mixture was sealed in a 15 mL Teflon-lined autoclave and heated under autogenous pressure to 160 °C for 72 h and then allowed to cool to room temperature naturally. After filtration, some saffron yellow schistose crystals were collected, washed with water, and then air dried (yield 63% based on Zn). Anal. calcd for C₂₆H₁₈N₂O₇Zn (1): C, 58.27%; H, 3.38%; N, 5.23%. Found: C, 58.59%; H, 2.99%; N, 5.37%. IR (KBr, cm⁻¹): 3084 (m), 3067 (w), 1661 (s), 1604 (s), 1559 (m), 1508 (m), 1479 (m), 1474 (m).

[Zn₂(CIA)(OH)(1,4-bibz)_{1.5}]·H₂O (2). ZnSO₄·7H₂O (0.029 g), 2-H₃CIA (0.016 g), and 1,4-bibz (0.015 g) were mixed with 3 mL buffer solvent (pH = 6) in a 25 mL Teflon-lined stainless steel container. The final mixture was sealed in a 15 mL Teflon-lined autoclave and heated under autogenous pressure to 160 °C for 72 h and then allowed to cool to room temperature naturally. After filtration, some yellow block crystals were collected, washed with water, and then air dried (yield 58% based on Zn). Anal. calcd for C₃₄H₂₆N₆O_{8.5}Zn₂ (2): C, 51.99%; H, 3.34%; N, 10.70%. Found: C, 52.15%; H, 3.03%; N, 10.52%. IR (KBr, cm⁻¹): 3129 (m), 1622 (s), 1593 (s), 1570 (m), 1542 (s), 1530 (m), 1463 (s), 1417 (m).

[Zn₂(CIA)(OH)(4,4'-bbpy)] (3). ZnSO₄·7H₂O (0.029 g), H₃CIA (0.016 g), and 4,4'-bbpy (0.015 g) were mixed with 3 mL buffer

solvent (pH = 6) and 1 mL methyl alcohol in a 25 mL Teflon-lined stainless steel container. The final mixture was sealed in a 15 mL Teflon-lined autoclave and heated under autogenous pressure to 160 °C for 72 h and then allowed to cool to room temperature naturally. After filtration, some yellow block crystals were collected, washed with water, and then air dried (yield 46% based on Zn). Anal. calcd for C₃₄H₂₄N₄O₈Zn₂ (3): C, 54.64%; H, 3.24%; N, 7.50%. Found: C, 54.42%; H, 3.31%; N, 7.73%. IR(KBr, cm⁻¹): 3129 (m), 3090 (w), 1570 (s), 1536 (m), 1519 (s), 1468 (s), 1417 (m).

[Zn(HCIA)(4,4'-bimp)]·H₂O (4). ZnSO₄·7H₂O (0.029 g), H₃CIA (0.016 g), and 4,4'-bimp (0.015 g) were mixed with 3 mL water, 0.3 mL NaOH (0.065 mol L⁻¹) and 1 mL isopropanol in a 25 mL Teflon-lined stainless steel container. The final mixture was sealed in a 15 mL Teflon-lined autoclave and heated under autogenous pressure to 160 °C for 72 h and then allowed to cool to room temperature naturally. After filtration, some brown block crystals were collected, washed with water, and then air dried (yield 46% based on Zn). Anal. calcd for C₃₆H₃₀N₄O₈Zn (4): C, 60.72%; H, 4.25%; N, 7.87%. Found: C, 60.54%; H, 34.66%; N, 7.68%. IR (KBr, cm⁻¹): 3129 (m), 3072 (w), 1622 (s), 1553 (s), 1525 (m), 1474 (s), 1434 (w), 1423 (w).

Crystal structure determination

Single-crystal X-ray diffraction analyses of the four complexes were carried out on a Bruker SMART APEX CCD diffractometer equipped with graphite monochromated Mo-K α radiation ($\lambda = 0.71073$ Å). Raw data were integrated with the SAINT program.¹⁷ The structures were solved by direct methods with SHELXS-97 and refined by full-matrix least-squares on F^2 using SHELXS-97.¹⁸ An empirical absorption correction was applied with the program SADABS.¹⁹ All the non-hydrogen atoms were refined anisotropically. The hydrogen atoms were set in the calculated positions and refined by a riding mode. The crystallographic details of complexes 1–4 are provided in Table 1, while the selected bond distances and angles are listed in Tables S1–S4.†

Sensing experiments

All the measurements were performed at room temperature. In order to improve the detection effect, the crystals were ground into a powder. The solid fluorescence of complexes 1–4 and



Table 1 Crystallographic data for complexes 1–4

Complex	1	2	3	4
Empirical formula	C ₂₆ H ₁₈ N ₂ O ₇ Zn	C ₃₄ H ₂₆ N ₆ O _{8.5} Zn ₂	C ₃₄ H ₂₄ N ₄ O ₈ Zn ₂	C ₃₆ H ₃₀ N ₄ O ₈ Zn
Formula weight	535.79	785.35	747.31	712.01
Space group	<i>P</i> 1	<i>P</i> 1	<i>P</i> 2(1)/ <i>n</i>	<i>P</i> 1
<i>a</i> /Å	7.4270(3)	10.203(4)	15.9212(16)	9.764(3)
<i>b</i> /Å	12.0551(5)	11.768(5)	11.5181(11)	11.687(3)
<i>c</i> /Å	13.0522(5)	14.073(6)	17.0439(17)	15.345(4)
α /°	82.5430(10)	86.764(7)	90	106.065(4)
β /°	86.4380(10)	80.749(6)	105.5296(16)	91.671(4)
γ /°	77.6410(10)	77.297(6)	90	102.175(3)
<i>V</i> /Å ³	1131.16(8)	1626.5(11)	3011.4(5)	1637.7(7)
Z, calculated density	2, 1.573 mg m ⁻³	2, 1.604 mg m ⁻³	4, 1.648 mg m ⁻³	2, 1.444 mg m ⁻³
Absorption coefficient	1.138 mm ⁻¹	1.540 mm ⁻¹	1.656 mm ⁻¹	0.810 mm ⁻¹
F(000)	548	800	1520	736
Theta range for data collection	2.982 to 27.509°	2.714 to 28.569°	2.481 to 28.298°	2.442 to 28.316°
Reflections collected/unique	23 964/5201	10 394/7641	18 485/7278	9856/7395
GOF	1.021	1.030	0.975	0.993
Final <i>R</i> indices [<i>I</i> > 2 sigma(<i>I</i>)]	<i>R</i> ₁ = 0.0440 <i>wR</i> ₂ = 0.1053	<i>R</i> ₁ = 0.0336 <i>wR</i> ₂ = 0.0743	<i>R</i> ₁ = 0.0380 <i>wR</i> ₂ = 0.0945	<i>R</i> ₁ = 0.0556 <i>wR</i> ₂ = 0.1229

ligands was determined. Overall, 18 different organic solvents: ethyl benzene (EB), formaldehyde (POM), *n*-pentane (NPE), 1,2-dichlorohydrin (DCE), isopropanol (IPA), ethanediol (EG), acetic ether (EAC), *n*-propyl alcohol (NPA), carbinol (MeOH), polyethylene glycol (PEG), benzene (PhH), *N,N*-dimethyl-formamide (DMF), cyclohexane (CYH), nitrobenzene (NB), acetonitrile (CH₃CN), 1,2-propanediol (PG), *n,n*-dimethylacetamide (DMA), and methyl alcohol (MtOH), were used in the sensing experiments. First, 3 mg of the complex and 10 mL water were added to the glass bottle, and the Zn-MOF suspension was obtained

after 1 h under ultrasonic treatment, and then left standing in air for 24 h. Then a stable suspension was formed, and the top liquid was utilized for fluorescence detection. To test the quenching properties of the complexes for nitrobenzene, 5 mL NB (5 mmol L⁻¹) was added to 2 mL of the suspension of the complexes in turn. The excitation wavelengths of complexes 1–4 were 305, 269, 285, and 267 nm with the excitation/emission slit widths of 5, 2.5, 2.5, and 5 nm, respectively. For all the fluorescence experiments, the emission spectra were recorded in the range of 350–650 nm.

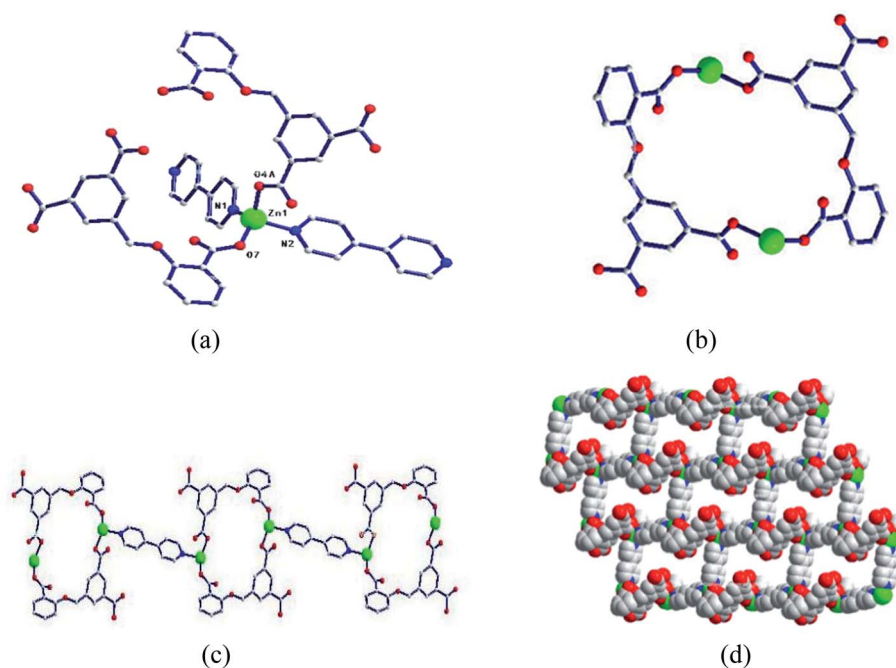


Fig. 1 (a) Coordination environment diagram of Zn ion in 1; (b) bimetallic ring; (c) one-dimensional chain based on a bimetallic unit ring; (d) two-dimensional network structure.



Results and discussions

Crystal structures

[Zn(HCIA)(4,4'-bipy)] (1). Single-crystal X-ray diffraction analysis showed that the central ion Zn1 was associated with two oxygen atoms (O4A, O7) of two HCIA²⁻ ligands, and two nitrogen atoms of two 4,4'-bipyridines (N1, N2) coordinated to form a four-coordinate tetrahedral configuration (the symmetry code is $(A) - x + 2, -y + 1, -z$) (Fig. 1a). The bond length of Zn–O

is 1.920–1.9470 Å and the bond length of Zn–N is 2.046–2.054 Å. The bond angle of N/O–Zn–O/N is 99.22–123.44°.

Two adjacent Zn ions form a bimetallic unit ring through two reverse bridges of HCIA²⁻ in the $\kappa_1:\kappa_1-\mu_2$ mode (Chart 2a), and the adjacent bimetallic unit ring is bridged by 4,4'-bipy to form a one-dimensional (1D) chain structure (Fig. 1b and c), with adjacent 1D chains vertically connected by 4,4'-bipy to form a two-dimensional (2D) brick-like network structure (Fig. 1d).

[Zn₂(CIA)(OH)(1,4-bibz)]_{1.5}·H₂O (2). The complex was based on a 2D network structure in which two 1D chains are interspersed. Single-crystal X-ray diffraction analysis showed that there are two crystallographic independent metallic Zn ions in the complex. The Zn1 ion is coordinated with two carboxyl oxygen atoms (O4, O7) of CIA³⁻ ligand, an oxygen atom (O8) of a hydroxyl group, and a nitrogen atom (N4) of an 1,4-bibz ligand to form a four-coordinated tetrahedral configuration (Fig. 2a). The central ion Zn₂ is coordinated with a carboxyl oxygen atom (O1) of a CIA³⁻ ligand, a hydroxyl oxygen atom (O8), and two nitrogen atoms (N1, N5) of two 1,4-bibz ligands. It also forms a four-coordinate tetrahedral configuration (Fig. 2b). The bond length range of Zn–O is 1.8848–2.005 Å, the bond length range of Zn–N is 2.000–2.0067 Å, the bond angle range of O–Zn–O is 104.64–115.54°, and the bond angles of O–Zn–N are in the range of 98.28–120.84°, and the bond angle of N–Zn–N is 110.05°.

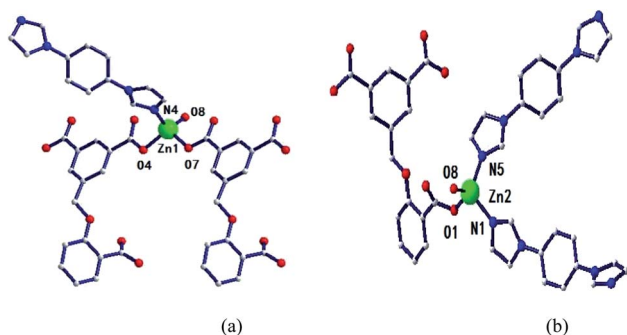


Fig. 2 Environmental coordination diagram of Zn₁ (a) and Zn₂ (b) ions in 2.

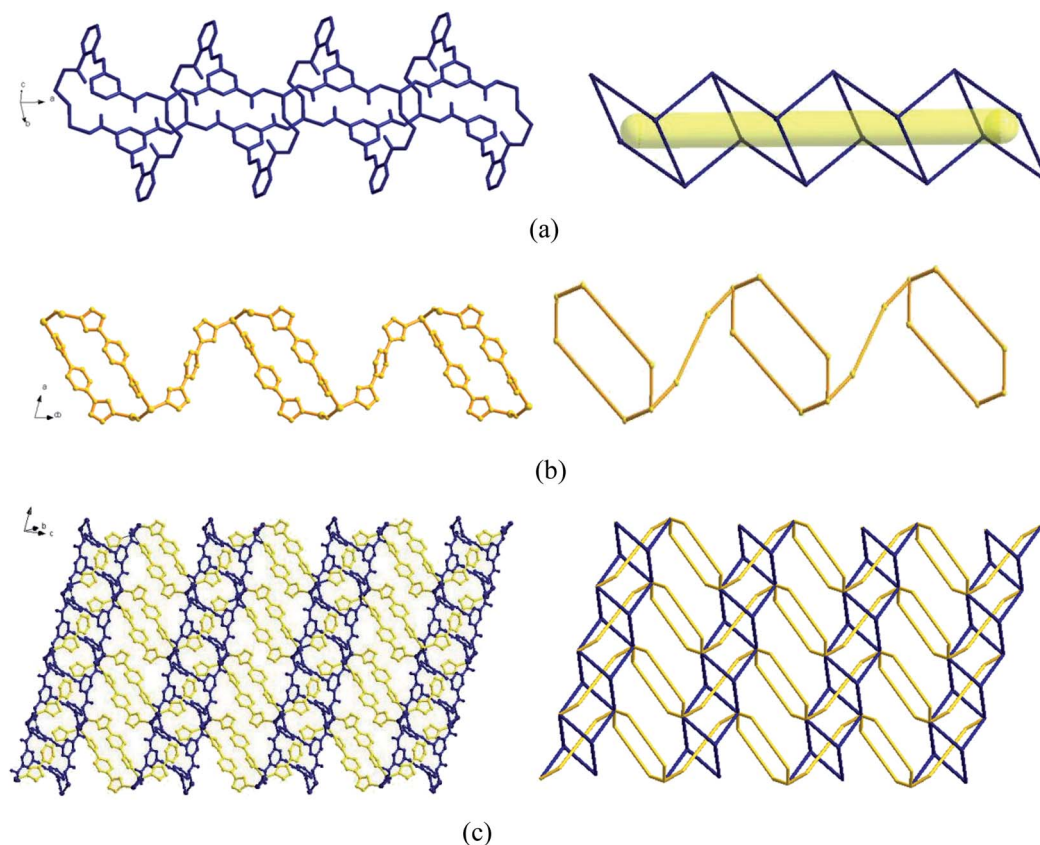


Fig. 3 (a) One-dimensional tubular structure formed by CIA³⁻ and a bimetallic unit and its simplified diagram; (b) one-dimensional chain structure formed by 1,4-bibz and a bimetallic unit and its simplified diagram; (c) two-dimensional interspersed structure and its simplified diagram.



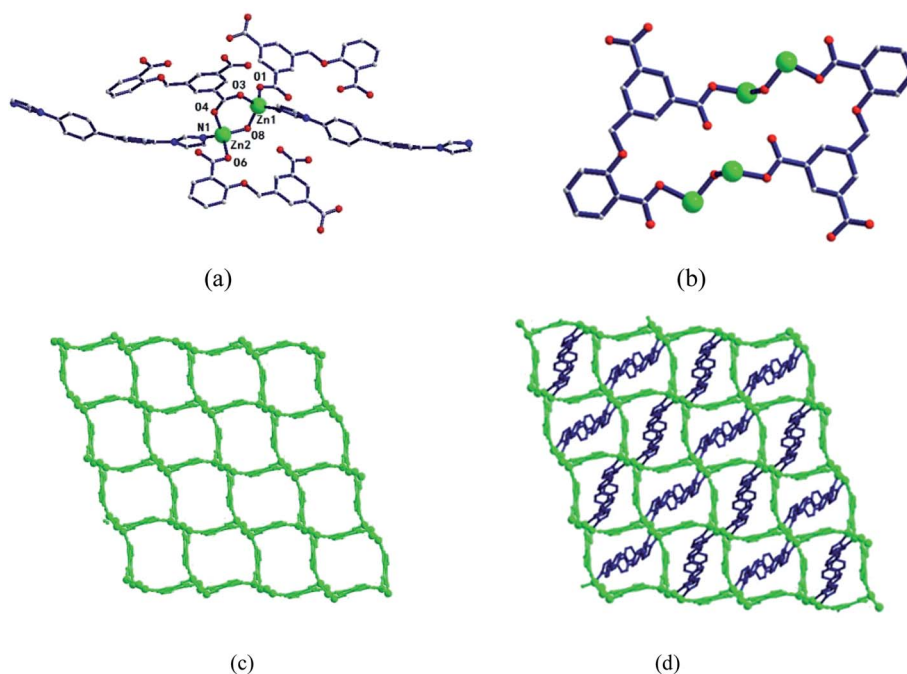


Fig. 4 (a) Coordination environment diagram of Zn ion in 3, (b) four-metal unit rings, (c) two-dimensional (4,4) network, (d) two-dimensional network structure.

In the complex, Zn₁ and Zn₂ ions form a bimetallic unit through the bridging effect of hydroxyl μ_2 -O, and the metal polyhedrons are connected by a common point. The CIA³⁻ ligand adopts the $\kappa_1:\kappa_1:\kappa_1-\mu_3$ coordination mode (Chart 2b) to bridge the bimetallic unit to form a 1D tubular structure A (Fig. 3a), and the auxiliary ligand 1,4-bibz is connected to form

a 1D wave chain structure B in a bidentate manner (Fig. 3b). Two types of 1D chains A and B are interspersed with each other, and are connected to form a 2D interspersed structure with bimetallic units as the nodes (Fig. 3c). The 2D interspersed structure is then stacked into a three-dimensional (3D) supramolecular structure through the π - π stacking force between the

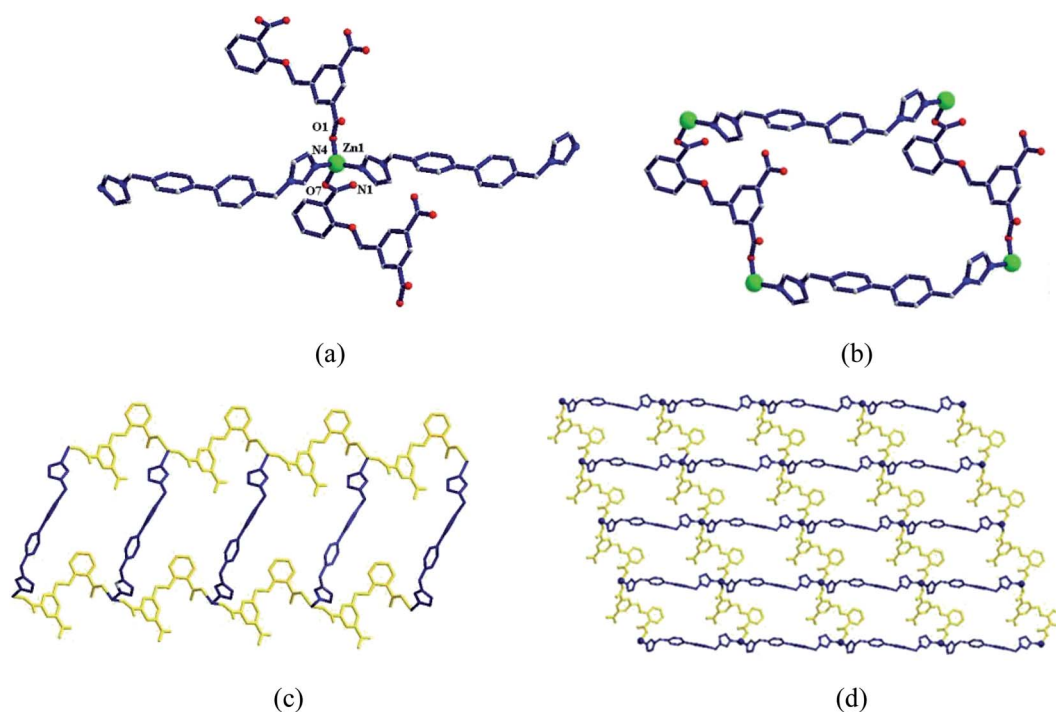


Fig. 5 (a) Coordination environment diagram of Zn ion in 4, (b) four-metal unit rings, (c) one-dimensional chain formed by a four-metal ring, (d) two-dimensional network structure.



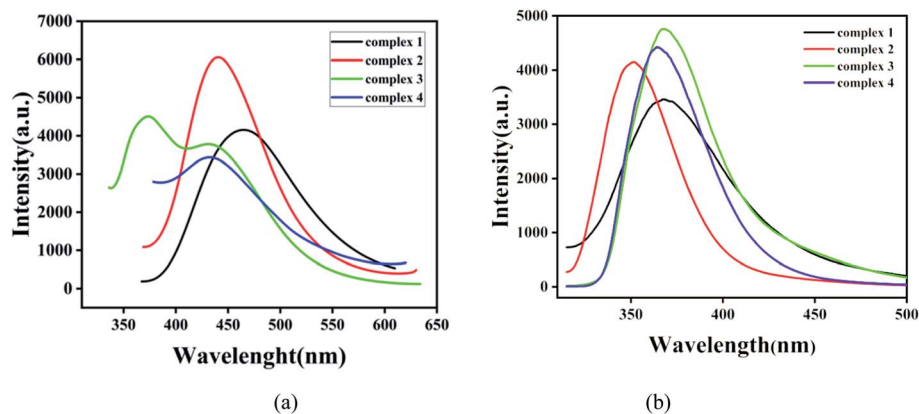


Fig. 6 Emission spectra of complexes 1–4 (a) in the solid state; (b) in the liquid state.

benzene ring of the CIA^{3-} ligand and the 1,4-bibz ligand (distance from point to surface: 3.869 Å).

[Zn₂(CIA)(OH)(4,4'-bbpy)] (3). Single-crystal X-ray diffraction analysis shows that the central atom Zn1 ion is associated with two oxygen atoms (O3, O1) of two CIA^{3-} ligands, one nitrogen atom (N4) of an 4,4'-bbpy ligand, and a hydroxyl oxygen atom (O8). The central ion Zn₂ ion is associated with two oxygen atoms (O4, O6) of the CIA^{3-} ligand, one nitrogen atom (N1) of an 4,4'-bbpy

ligand, and an oxygen atom of a hydroxyl molecule (O8), forming two opposite triangular cones (Fig. 4a). The bond length range of Zn–O is 1.925–2.024 Å, the bond length range of Zn–N is 2.004–2.024 Å, the bond angle range of O–Zn–O is 101.91–117.11°, and the bond angle range of O–Zn–N is 96.68–119.59°.

Two metal ions (Zn₁, Zn₂) are connected by the hydroxyl oxygen atom (O8) and two CIA^{3-} ligands in the $\kappa_1:\kappa_1:\kappa_1:\kappa_1-\mu_4$ mode (Chart 2c) reversely to form a four-metal unit ring

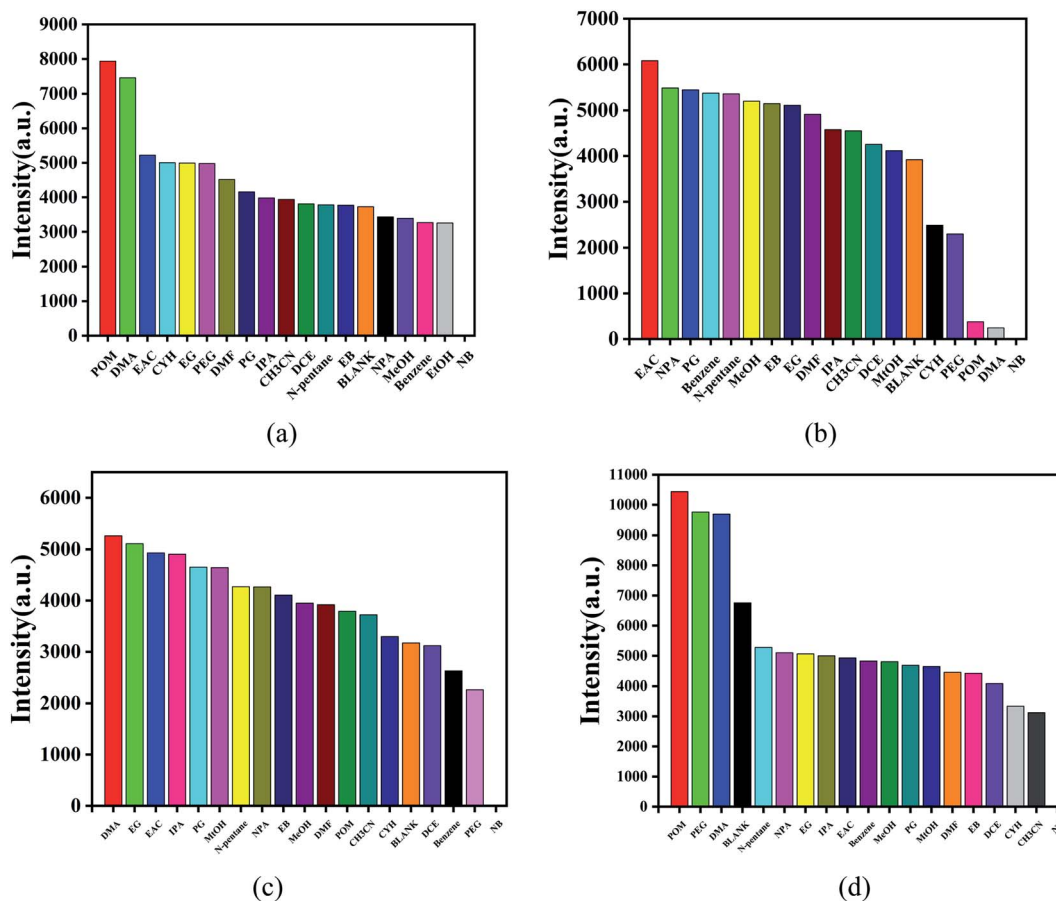


Fig. 7 Fluorescence qualitative selection for different organic solvents of complexes.



(Fig. 4b). The four-metal unit rings extend into a 1D chain by CIA^{3-} ligands bridging (Fig. S1†). The 2D (4,4) network is constructed from the 1D chains based on CIA^{3-} ligands (Fig. 4c). The nitrogen atoms of 4,4'-bbpy are coordinated to Zn^{2+} ions and occupy the back and forth positions in the metal unit rings and contribute to the formation of the 2D network structure (Fig. 4d).

[Zn(HCIA)(4,4'-bimp)]·H₂O (4). Single-crystal X-ray diffraction analysis showed that the central ion Zn1 ion is coordinated to two oxygen atoms (O1, O7) of two HCIA^{2-} ligands, and two nitrogen atoms (N1, N4) of 4,4-bis coordinate to form a four-coordinated tetrahedral configuration (Fig. 5a). The bond length scope of Zn–O is 1.938–1.962 Å and the bond length of Zn–N is 1.986–2.029 Å. The bond angles of O/N–Zn–O/N range from 96.88 to 120.06°.

Four adjacent Zn^{2+} ions are connected by two CIA^{2-} ligands in the $\kappa_1:\kappa_1-\mu_2$ mode (Chart 2d) and two 4,4-bimp ligands alternately form a four-metal ring (Fig. 5b). The four-metal rings continue to expand to a ladder-like chain (Fig. 5c), which extends into a 2D network structure (Fig. 5d).

Thermogravimetric analysis (TGA)

Based on the structural diversity of these complexes, we carried out thermogravimetric analysis in an air atmosphere at a heating rate of $10\text{ }^\circ\text{C min}^{-1}$ from $30\text{ }^\circ\text{C}$ to $900\text{ }^\circ\text{C}$ to investigate the thermal stabilities (Fig. S2†). As seen from the curve of complex 1, the thermal decomposition process begins from a platform in the temperature range of $30\text{ }^\circ\text{C}$ to $332\text{ }^\circ\text{C}$, which indicates the complex could be stable before $332\text{ }^\circ\text{C}$. Then a large weight loss

process takes place, which could be attributed to the fracture of the complex skeleton. Until $868\text{ }^\circ\text{C}$, the curve tends to be smooth and the process is finished. For 2, the process was divided into two steps: the first weight loss rate was 2.92% from $30\text{ }^\circ\text{C}$ to $73\text{ }^\circ\text{C}$, which might be due to the loss of a coordination water molecule (calcd: 2.29%); and then from $73\text{ }^\circ\text{C}$ to $346\text{ }^\circ\text{C}$, there is a platform, which indicates the stable stage of dehydrated Zn-MOF. The second large weight loss process from $346\text{ }^\circ\text{C}$ corresponds to the collapse of the complex skeleton. After a slight weight loss, the one-step large thermal decomposition of complex 3 occurs from $380\text{ }^\circ\text{C}$ to $866\text{ }^\circ\text{C}$, ascribed to the collapse of the complex framework. The decomposition process of 4 was divided into two steps: first, the weight loss rate was 2.73% from $30\text{ }^\circ\text{C}$ to $113\text{ }^\circ\text{C}$, which could be due to the loss of a coordination water molecule (calcd: 2.53%); and then a final large weight loss process happens from $290\text{ }^\circ\text{C}$, which could be related to the skeleton destruction of the complex, until about $800\text{ }^\circ\text{C}$.

In order to confirm the phase purity of the bulk materials of 1–4, powder X-ray diffraction (PXRD) patterns were recorded at room temperature (Fig. S3†). Compared to the simulated patterns from the single-crystal data, we could conclude that the bulk as-synthesized crystalline materials represented the complexes due to their adequate similarity.

Luminescence spectra in the solid state and in the liquid state

In order to investigate the luminescence properties of complexes 1–4, the solid-state photoluminescent spectra of

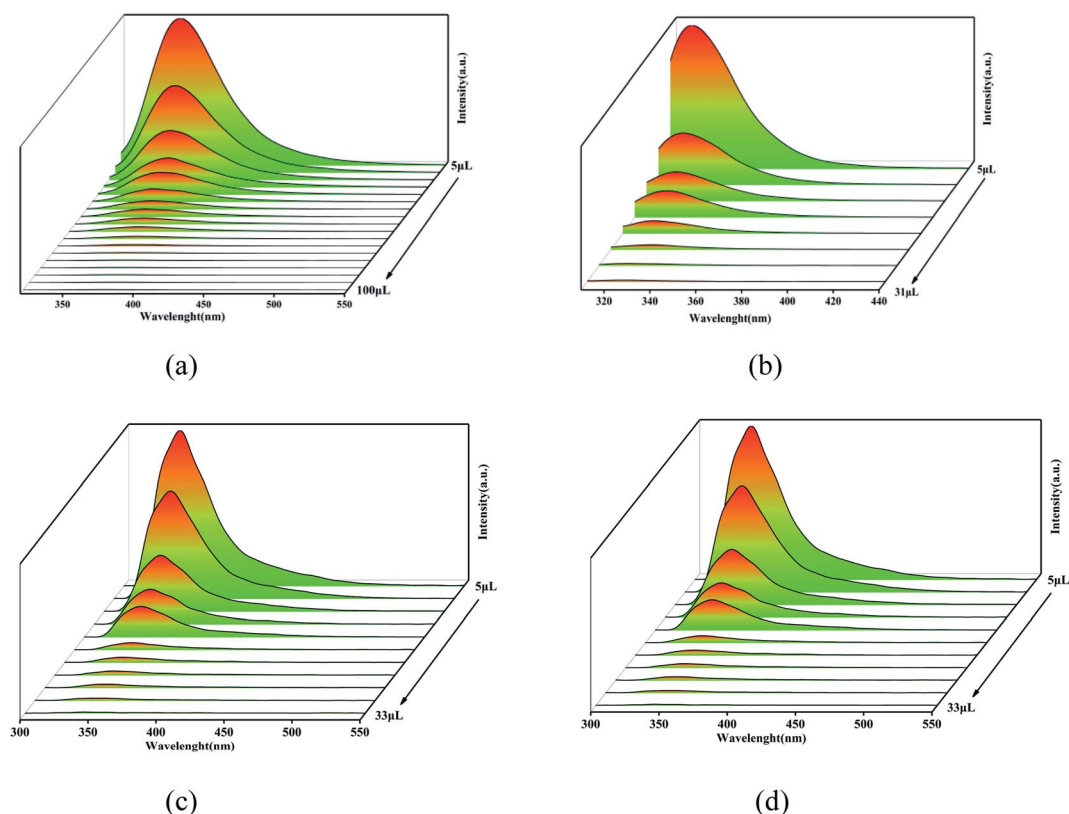


Fig. 8 Concentration-dependent luminescence quenching of complexes 1 (a), 2 (b), 3 (c), and 4 (d) suspensions in water by nitrobenzene (NB).



these complexes and free ligands (H_3CIA , 4,4'-bipy, 1,4-bibz, 4,4'-bbpy, 4,4'-bimp) were performed on a F7100 spectrofluorophotometer at room temperature. The emission of the free ligands (H_3CIA , 4,4'-bipy, 1,4-bibz, 4,4'-bbpy, 4,4'-bimp) are displayed in Fig. S4.† For the free ligand H_3CIA , the maximum peak was centered at 321 nm ($\lambda_{ex} = 361$ nm), while the N-donor auxiliary ligands 4,4'-bipy, 1,4-bibz, 4,4'-bbpy, 4,4'-bimp had emission peaks at 474 nm ($\lambda_{ex} = 390$ nm), 322 nm ($\lambda_{ex} = 280$ nm), 403 nm ($\lambda_{ex} = 264$ nm), and 342 nm ($\lambda_{ex} = 302$ nm), respectively. As shown in Fig. 6a, the emission spectra of complexes 1–4 exhibited different peaks from the free ligands. For 1, there was one broad and strong peak at 465 nm ($\lambda_{ex} = 315$), which could be mainly attributed to the $\pi \rightarrow \pi^*$ transition of 4,4'-bipy, compared with those of the free ligands H_3CIA and 4,4'-bipy. The emission peak of 2 was also a single broad and strong peak at 440 nm ($\lambda_{ex} = 322$ nm), which arises with a large red-shift from the ligands H_3CIA and 1,4-bibz, but it should belong to the intra-ligands transition of the organic ligands. The emission main peak at 373 nm and one shoulder peak at 430 nm ($\lambda_{ex} = 326$ nm) of 3 were closer to that of 4,4'-bbpy, and complex 4 with one peak at 432 nm ($\lambda_{ex} = 321$ nm), which was higher than those of H_3CIA and 4,4'-bimp ligands, which all could be due to the $\pi \rightarrow \pi^*$ transitions of the organic ligands. The emission spectra of 1–4 in suspension aqueous solution

were investigated and the results shown in Fig. 6b, which slightly differ from those in the solid state due to the effect of the solvent. The excitation spectra of complexes 1–4 are exhibited in Fig. S5.†

Nitrobenzene explosive sensing

Nitrobenzene is an organic synthesis intermediate and is used as a raw material for producing aniline, and so is widely used in the organic synthesis industry. However, nitrobenzene is highly toxic, causing great harm to humans and biological environments, so the rapid detection of nitrobenzene is of great significance. Mixtures of the powders of complexes 1–4 (3 mg) and water (10 mL) were treated by an ultrasonic method for 1 h and then left standing in air for 24 h to form the suspension of the MOF aqueous solution. Then a stable suspension was formed, and the top liquid was utilized for fluorescence detection. Here, 1 mL of the supernatant of complexes 1–4 were taken and added to 20 μ L different pure organic solvents with vigorous shaking for fluorescence study. Then the fluorescence qualitative analysis was carried out.

For complex 1, 370 nm specific intensity of electron transition emission was selected to evaluate the fluorescence response at the excitation of 305 nm (Fig. 7a). In Fig. 7b, for complex 2, the electron transition emission ratio intensity of

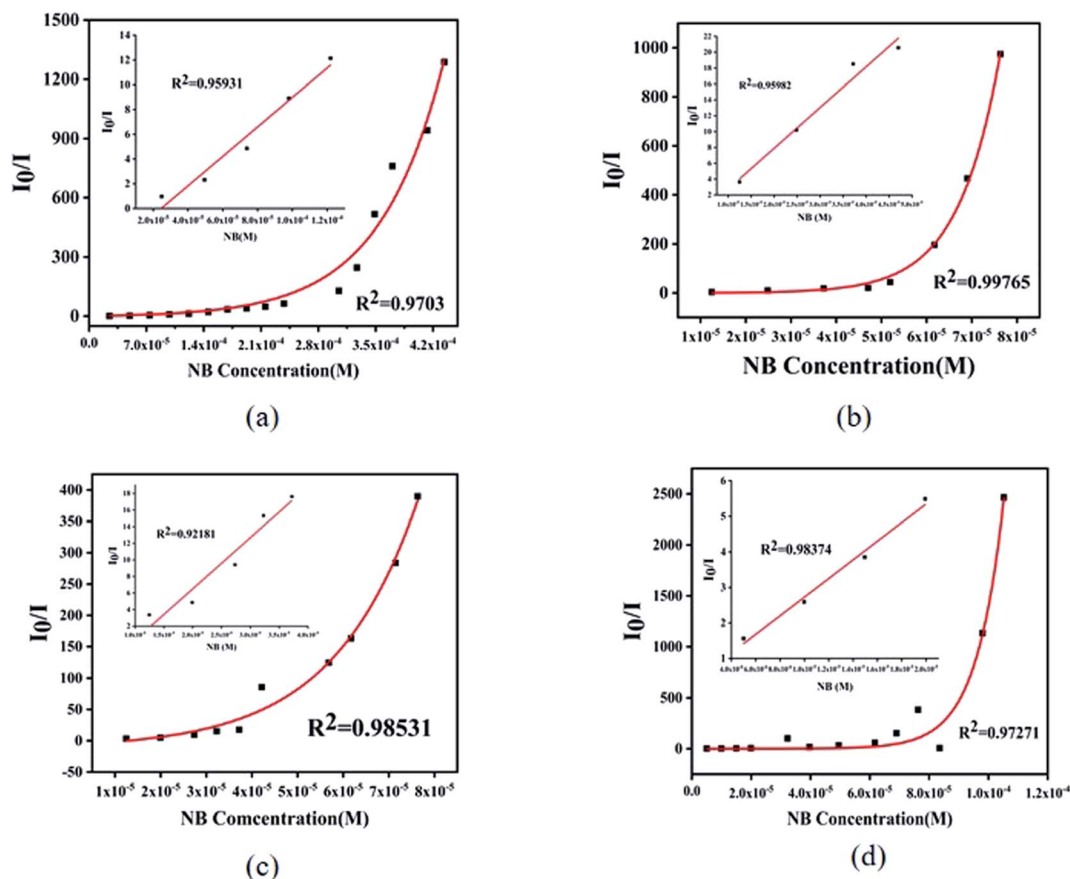


Fig. 9 Exponential function of fluorescence quantitative detection of complexes 1 (a), 2 (b), 3 (c), and 4 (d) suspensions in water quenched by nitrobenzene (NB) (inset: linear S–V plot of I_0/I vs. NB in low concentration intervals).



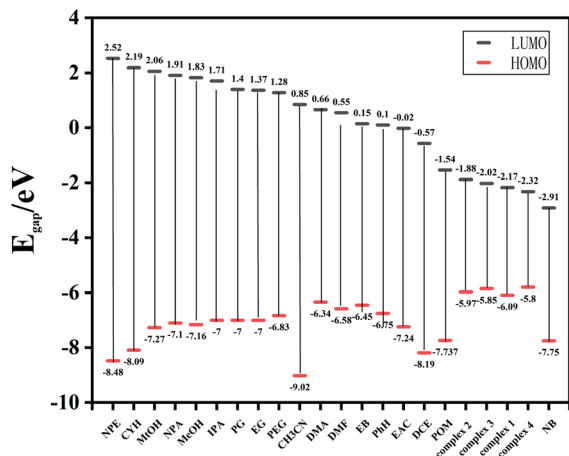


Fig. 10 HOMO–LUMO energy levels and molecular frontier orbital energy–level diagram of each organic solvent and complexes 1–4.

327 nm was selected to evaluate the fluorescence response under 269 nm excitation. As shown in Fig. 7c, for complex 3, the specific intensity of electron transition emission at 348 nm was selected to evaluate the fluorescence response at an excitation of 285 nm. For complex 4, the specific intensity of electron transition emission at 267 nm was selected to evaluate the fluorescence response when excited at 305 nm (Fig. 7d). The characteristic fluorescence emission intensity was obviously affected by the series of organic molecules, especially nitrobenzene. For all the complexes, the mixtures containing nitrobenzene showed a complete quenching effect, and complex 4 had the highest selectivity for nitrobenzene than the other complexes, as shown in Fig. 7.

For further analysis, all the complexes were quantitatively analyzed with nitrobenzene (NB) to gain a deeper understanding of the sensing properties. Then NB with a concentration of 5 mmol L⁻¹ ethanol solution was added in the suspension of complex 1 (1 mL) and complexes 2–4 (2 mL) in turn, respectively, to measure the change in fluorescence intensity. As the volume of NB solution increased, the fluorescence emission intensity of 1–4 decreased gradually (Fig. 8). For complex 1, when 5 μ L NB was added, the luminescence intensity was quenched by 43%. When 105 μ L NB was added, the luminescence intensity was quenched absolutely. In addition, a dose–response diagram in the whole titration region was found to be ideally consistent with the exponential function I_0/I

$= -5.25 \times (1 - e^{12719.02[\text{NB}]})$ (where I_0 and I represent luminescence intensities of water suspension of complex 1 before and after exposure to NB, respectively). Besides, a good linear correlation ($R^2 = 0.9703$) was observed in the concentration range 0–0.098 mM with the quenching constant K_{SV} of $1.19 \times 10^5 \text{ M}^{-1}$ (Fig. 9a inset). The detection limit (LOD) for NB was $1.47 \times 10^{-7} \text{ M}$ as calculated by $3\delta/K_{\text{SV}}$, where δ is the standard deviation of the repeated detections of the bare solutions. For complex 2, the luminescence intensity quenched reached 73% when 5 μ L nitrobenzene was added and then was completely quenched with 34 μ L. Furthermore, the dose–response diagram in the entire titration area was ideally consistent with the exponential function $I_0/I = -0.24 \times (1 - e^{108716.14[\text{NB}]})$. In addition, a good linear correlation ($R^2 = 0.9598$) was observed in the concentration range 0–0.074 mM, where the quenching constant K_{SV} was $5.127 \times 10^5 \text{ M}^{-1}$ (Fig. 9b inset), and the detection limit (LOD) for NB of 2 was $1.42 \times 10^{-7} \text{ M}$. For complex 3, the luminescence intensity quenched was 70% when 5 μ L NB was added, and was then completely quenched with 35 μ L NB. The dose–response diagram in the entire titration area was ideally consistent with the exponential function $I_0/I = 6.29 \times e^{-[\text{NB}]/-1.84 \times 10^5 - 12.54}$. In addition, a good linear correlation ($R^2 = 0.9218$) was observed in the concentration range 0–0.037 mM, where the quenching constant K_{SV} was $6.18 \times 10^5 \text{ M}^{-1}$ (Fig. 9c inset), and the detection limit (LOD) for nitrobenzene was $3.03 \times 10^{-8} \text{ M}$. When 2 μ L NB was added, the luminescence intensity of complex 4 was quenched by 36% and was then quenched absolutely when 43 μ L nitrobenzene was added. In addition, the dose–response diagram in the whole titration region was ideally consistent with the exponential function $I_0/I = 0.03 \times e^{108757.11[\text{NB}]}$. A good linear correlation ($R^2 = 0.9837$) was observed in the concentration range 0–0.0199 mM, with the quenching constant K_{SV} as $2.62 \times 10^5 \text{ M}^{-1}$ (Fig. 9d inset), and the detection limit (LOD) for nitrobenzene was $1.92 \times 10^{-7} \text{ M}$.

To elucidate the highly selectivity of complexes 1–4 for NB, the mechanism of fluorescence quenching was investigated. After 4 weeks of dispersion in deionized water, the fluorescence intensity of the suspension of the Zn-MOFs aqueous solution almost did not decrease, which might mean there was no obvious structural collapse, thus showing the stability of the Zn-MOFs in water (Fig. S5[†]). As shown in Fig. S6,[†] the PXRD patterns of the samples soaked and not soaked in nitrobenzene solutions were similar, indicating that the structure collapse might not be the main reason for the fluorescence quenching.

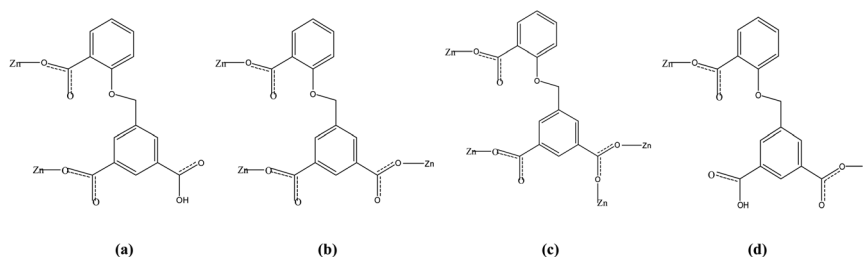


Chart 2 Coordination modes of the H₃CIA ligands used in complexes 1–4.



Generally, there are three factors that lead to the fluorescence quenching behavior of fluorescent materials: structural change, photoinduced electron transfer (PET), and energy transfer. By Density Functional Theory, we calculated the frontier orbitals (HOMO and LUMO) energy levels of various organic solvents and complexes 1–4 (Fig. 10). From the calculated results, we found the other organic solvents possessed a higher LUMO energy level than complexes 1–4, except from NB. The lower the LUMO energy of the analyte is, the easier the transition of the excited-state electrons is. Thus, the electron may transfer from the framework to the NB under photo-induction, which is considered as the PET effect causing the fluorescence quenching of NB.²⁰

Conclusions

A series of Zn-MOFs were prepared hydrothermally with 5-(2-carboxy-benzyloxy) isophthalic acid (H₃CAI) and four linear N-donor ligands. Complexes 1–4 exhibited 2D networks with different features resulting from the different coordination modes of the H₃CAI ligand and different linear N-donor ligands. The thermal stabilities and fluorescent properties of all the complexes were investigated in the solid state. The fluorescent detection of organic solvents revealed that all the Zn-MOFs could highly sensitively and selectively detect nitrobenzene in aqueous solution with LOD values of 0.147 μM (1), 0.142 μM (2), 0.0303 μM (3), and 0.192 μM (4), which means these MOF materials might be used as the sensor for nitrobenzene in the future. The PET effect might be the main reason for the fluorescence quenching of NB, as verified by the theoretical calculation.

Conflicts of interest

There are no conflicts to declare.

Acknowledgements

This work was supported by National Natural Science Foundation of China (No. 22063010 and 21763028).

Notes and references

- 1 Y. Liu, X. Xie, C. Cheng, Z. Shao and H. Wang, *J. Mater. Chem. C*, 2019, **7**, 10743–10763.
- 2 I. Takayuki, K. Takashi, M. Shin-ichi, N. Takashi, Y. Kizashi and I. Hiizu, *Dalton Trans.*, 2002, 3177–3186.
- 3 A. Mahsa, R. J. Niu, W. H. Zhang and I. P. Lang, *Polyhedron*, 2018, **153**, 218–225.
- 4 D. S. Liu, M. Li, X. C. Li and F. J. Ren, *Chem. Eng. J.*, 2020, **387**, 124008–124011.
- 5 S. A. A. Razavi and A. Morsali, *Coord. Chem. Rev.*, 2020, **415**, 213299–213342.
- 6 S. Shirin, W. Jun and C. J. Peter, *J. Solid State Chem.*, 2020, **293**, 121762–121763.
- 7 J. K. Ying, L. Dong, H. L. Yue and H. C. Guang, *J. Solid State Chem.*, 2019, **278**, 120891–120892.
- 8 Y. Zhou, Q. Yang, D. N. Zhang, N. Gan and Q. Li, *Sens. Actuators, B*, 2018, **261**, 137–143.
- 9 X. Lian and B. Yan, *Sens. Actuators, B*, 2019, **281**, 168–174.
- 10 X. Y. Xu, B. Yan and X. Lian, *Nanoscale*, 2018, **10**, 13722–13729.
- 11 S. S. Zhao, J. Yang, Y. Y. Liu and J. F. Ma, *Inorg. Chem.*, 2016, **55**, 2261–2273.
- 12 R. W. Corkery, *Curr. Opin. Colloid Interface Sci.*, 2008, **134**, 288–302.
- 13 (a) Z. C. Hu, B. J. Deibert and J. Li, *Chem. Soc. Rev.*, 2014, **43**, 5815–5840; (b) K. Vellingiri, D. W. Boukhyalov, S. K. Pandey, A. Deep and K. H. Kim, *Sens. Actuators, B*, 2017, **245**, 305–313; (c) E. Holmgren, H. Carlsson, P. Goede and C. Crescenzi, *J. Chromatogr. A*, 2005, **1099**, 127–135; (d) S. S. Li, J. H. Fang, L. Li, M. Zhu, F. Zhang, B. Y. Zhang, T. J. Jiang and Y. X. Zhang, *Talanta*, 2021, **225**, 122087.
- 14 (a) Z. Sun, J. Sun, L. Xi, J. Xie, X. F. Wang, Y. Ma and L. C. Li, *Cryst. Growth Des.*, 2020, **20**, 5225–5234; (b) S. L. Sun, X. Y. Sun, Q. Sun, E. Q. Gao and L. Li, *J. Solid State Chem.*, 2020, **292**, 121701–121708; (c) Y. H. Yang, G. J. Ren, W. H. Li, D. X. Gu, Z. Q. Liang, Y. F. Liu and Q. H. Pan, *Polyhedron*, 2020, **185**, 114599–114606; (d) L. R. Yang, C. Lian, X. F. Li, Y. Y. Han, L. L. Yang, T. Cai and C. Y. Shao, *ACS Appl. Mater. Interfaces*, 2017, **9**, 17208–17217.
- 15 C. B. Fan, X. Zhang, N. N. Li, C. G. Xu, R. X. Wu, B. Zhu, G. L. Zhang, S. Y. Bi and Y. H. Fan, *J. Pharm. Biomed. Anal.*, 2020, **188**, 113444–113458.
- 16 (a) S. J. Wang, H. L. Wu, L. X. You, G. Xiong, Y. K. He, F. Ding and Y. G. Sun, *Inorg. Chim. Acta*, 2019, **485**, 49–51; (b) J. Z. Gu, Y. Cai, M. Wen, Z. F. Shi and A. M. Kirillov, *Dalton Trans.*, 2018, **47**, 14327–14339; (c) X. Mi, D. Sheng, S. Wang, J. Lu, L. Yang and Z. Zhou, *Acta Crystallogr., Sect. C: Struct. Chem.*, 2019, **75**, 657–666.
- 17 SAINT-Plus, version 6.02, Bruker Analytical X-ray System, Madison, WI, 1999.
- 18 (a) Bruker AXS, Inc., Madison, WI, 2013; (b) G. M. Sheldrick, *Acta Crystallogr., Sect. A: Found. Crystallogr.*, 2008, **64**, 112–122; (c) X-SHELL, version 4.01 and SHELXTL, version 6.10; (d) Bruker AXS, Inc., Madison, WI, 2000.
- 19 G. M. Sheldrick, *SADABS, Program for Empirical Absorption Correction of Area Detector Data*, University of Göttingen, Germany, 1996.
- 20 G. Qin, J. Wang and L. Li, *Talanta*, 2020, **221**, 121421.

